ORIGINAL RESEARCH

# Improvement of platelet aggregation and rapid induction of hemostasis in chitosan dressing using silver nanoparticles

**Guangqian Lan · Qing Li · Fei Lu · Kun Yu · Bitao Lu · Rong Bao · Fangyin Dai**

**Abstract** There is an increasing demand for high-performance hemostatic agents with good antibacterial efficiency and biocompatibility. In this study, a chitosan/gelatin/sodium hyaluronate hemostatic dressing with silver nanoparticles (CGSH/Ag50) was designed and characterized. Our results suggest that CGSH/Ag50 has high blood absorption and promotes platelet aggregation by the activation of positively charged surface and stimulation of silver nanoparticles. Owing to these excellent properties, CGSH/Ag50 could rapidly control hemorrhage in rabbit ear and liver injury models. CGSH/Ag50 also shows good antibacterial activity, good liquid absorption, and significantly promotes full-thickness wound healing. In the hemolysis and L929 cell cytotoxicity assays, CGSH/Ag50 exhibited no cytotoxicity, suggesting good hemocompatibility and biocompatibility. These observations suggest that CGSH/Ag50 can be an efficient hemostatic material with enough biocompatibility to be used for controlling hemorrhage and promoting wound healing after hemostasis surgery.

**Keywords** Hemostasis · Silver nanoparticles · Wound healing · Antibacterial activity · Chitosan

Guangqian Lan and Qing Li have equally contributed to this work.

G. Lan (✉) · Q. Li · F. Lu · K. Yu · B. Lu · F. Dai
State Key Laboratory of Silkworm Genome Biology,
College of Textile and Garments, Southwest University,
Chongqing 400715, China
e-mail: 30353930@qq.com

G. Lan · F. Lu · F. Dai
Chongqing Engineering Research Center of Biomaterial
Fiber and Modern Textile, Chongqing 400715, China

R. Bao
The Ninth People's Hospital of Chongqing,
Chongqing 400715, China

## Introduction

Hemorrhagic trauma is inevitable in daily life, however, over 30% blood loss in a short period of time can be life threatening (Nie et al. 2018; Sakoda et al. 2018; Wang et al. 2018). Traditional hemostatic material, such as cotton gauze, triangle towel, and cotton pads are not ideal for irregularly shaped wounds, like deep and narrow bleeding points or ruptured arteries and veins (Sun et al. 2017). Meanwhile, in traumatic bleeding surgery, wound infection by microorganisms is a potential risk to patients (Zhao et al. 2017; Zhu et al. 2018). If the wound is infected by bacteria, the blood clot in the extracellular matrix becomes a hotbed for bacterial breeding, thus causing inflammation of the wound and affecting wound healing (Gowda et al. 2015; Rodriguez-Menocal et al. 2015). Therefore, preparing new hemostatic material, which has multiple functions of hemostasis, antibacterial activity, stimulating cell division and differentiation,

and accelerating tissue healing is urgently required for biomedical applications.

In order to design a hemostatic composite with antimicrobial properties that can promote wound healing, a substrate with inherent functions of hemostasis and antibacterial property is preferred. Chitosan (CS), is obtained after the partial deacetylation of chitin. Chitosan exhibits good water absorption, antimicrobial activity, biocompatibility, blood compatibility, and many other properties (Jin et al. 2018; Liang et al. 2016; Shi et al. 2016, 2017). Additionally, chitosan can induce aggregation of red blood cells and platelets for controlling hemorrhage owing to its inherent positive potential (Hattori and Ishihara 2017; Shimojo et al. 2016). Therefore, chitosan has been widely researched as surgical biomaterial for hemostasis (Seon et al. 2017), in products such as Hemcon bandage and KytoCel (Hu et al. 2018). However, the applications of chitosan are restricted by its inability to absorb blood rapidly for controlling large hemorrhages (Hu et al. 2018), and by the fact that its antibacterial activity only occurs in solution (Mitra et al. 2016). Together, it can be acknowledged that developing an ideal chitosan-based hemostatic material with good blood absorbing and antibacterial properties is challenging.

Chitosan has been widely researched with other natural polymer composites to improve its liquid absorption (Lu et al. 2017; Sarhan et al. 2016; Zhang et al. 2018). Gelatin is one such polymer (Seon et al. 2017), which is often used for drug release, preparation of artificial bones and skin, and other tissue engineering (Wang et al. 2017; Zhao et al. 2016). Because of the presence of –NH$_2$, –OH, –COOH active groups in the molecular structure of gelatin, it can be combined with chitosan molecules through hydrogen or ionic bonds, to form a stable interpenetrating network structure for holding liquid (Kovach et al. 2016). Additionally, gelatin has been reported to have hemostatic effects of aggregating and activating platelets (Man 2018; Seon et al. 2017). Sodium hyaluronate, a natural polysaccharide, has also been widely studied as a biomaterial for compounding with chitosan because of its ability to control hydration in repairing tissues (Abdel-Rahman et al. 2016; Berce et al. 2018). Therefore, it is hypothesized that compounding chitosan with gelatin or sodium hyaluronate could improve its liquid absorption capacity.

The antibacterial property of chitosan applying in biotechnology may be broadened by combining chitosan with metal nanoparticles (Hu et al. 2018; Ma et al. 2017). Owing to their quantum effect, small size and enormous specific surface area, silver nanoparticles (Ag NPs) exhibit good antibacterial activity against gram-negative and gram-positive bacteria, which has been widely used in medical applications (Xia et al. 2018; Yoo et al. 2018). However, the further application of Ag NPs is limited by their aggregation, which can result in cellular cytotoxicity (Bonaventura et al. 2018). Modifying Ag NPs with gelatin could remove this restriction. Gelatin contains –NH$_2$ and –OH groups, which can reduce Ag$^+$ to Ag NPs and form protective layers on the NP surface. Thus, Ag NPs can exist in gelatin solution without aggregating (Chang et al. 2018) to exert efficient antibacterial activity and cytocompatibility. Additionally, Ag NPs have been reported to promote blood clotting by aggregating and activating platelets. Smock et al. found that Ag NPs can activate platelets and promote the generation of thrombin (Smock et al. 2014), meanwhile, Jun et al. reported that Ag-NPs can accelerate thrombin generation by inducing platelet aggregation and increasing phosphatidylserine exposure (Jun et al. 2011). Inspired by these premises, we combined Ag NPs with chitosan, gelatin, and sodium hyaluronate to design an efficient hemostatic material in this study. The chitosan/gelatin/sodium hyaluronate/Ag NP hemostatic sponge was generated using freeze-drying technology, and its hemostatic properties were evaluated in vitro and in vivo.

## Materials and methods

### Materials

Chitosan (molecular weight: 10,000 Da, degree of acetylation: 85%) and gelatin type A (porcine, bloom 300) were purchased from Sigma-Aldrich (St. Louis, MO, USA). Silver nitrate (AgNO$_3$) and sodium hyaluronate were obtained from Kelong Chemical.

Reagent (Chengdu, China). All other chemicals were purchased from Sigma-Aldrich and used as received, if not specified. New Zealand white rabbits were obtained from the Animal Laboratory Center of Third Military Medical University. Animal experiments were performed according to institutional
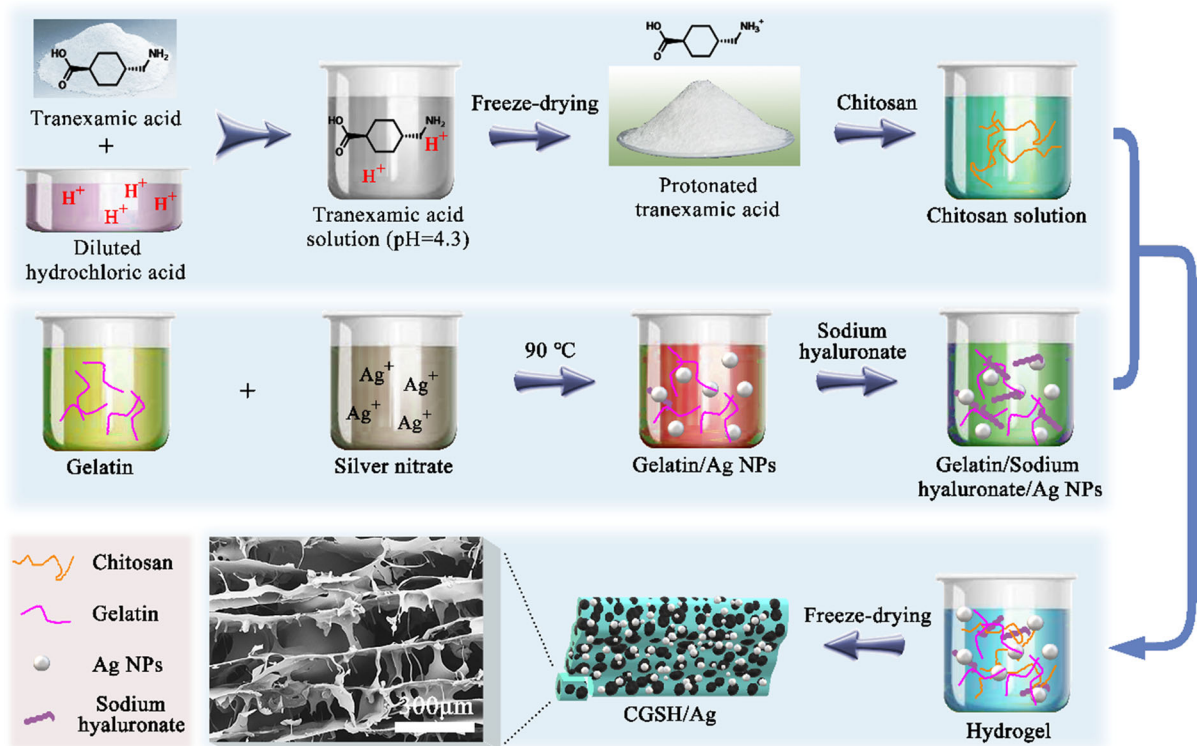
**Scheme 1** Conceptual representation of the preparation of CGSH/Ag. TA-NH$_3^+$ powder was prepared to dissolve the chitosan. Gelatin was employed to prepare evenly distributed Ag NPs, following which sodium hyaluronate was added. CGSH/Ag was prefabricated by compounding the two obtained mixtures and freeze-drying as hemostatic material

ethical use protocols. Anticoagulant blood was prepared by blending heart blood of rabbits with 3.8% sodium citrate at a volume ratio of 9:1. Platelet poor plasma (PPP) was collected by centrifugation at 4000 rpm for 15 min at 37 °C. Anticoagulant blood was centrifuged at 2500 rpm for 10 min to obtain platelet rich plasma (PRP).

### Preparing hemostatic material

Protonated tranexamic acid (TA-NH$_3^+$) was prepared by adding HCl to a tranexamic acid (TA-NH$_2$) solution to adjust the pH to 4.3, and freeze dried (Baylis et al. 2015). Six grams TA-NH$_3^+$ powder and 6 g chitosan were added to 100 mL deionized water and stirred for 5 min to obtain the chitosan solution. To prepare equably dispersed Ag NPs, 1 g gelatin was dissolved in 100 mL deionized water, to which sliver nitrate solution was dropped and incubated at 90 °C for 5 h. 2 g sodium hyaluronate was added to the obtained flaxen gelatin/Ag NPs solution, followed by

the equable mixing of prepared chitosan solution. The final ratios of Ag NO$_3$ in the whole solution were set to 10, 20, 30, 40, 50, 60, 70, 80, 90, 100, 200, or 300 μg/g. Lyophilization was carried out to obtain chitosan/gelatin/sodium hyaluronate/Ag NP (CGSH/Ag) sponge. The preparation of CGSH/Ag is presented in Scheme 1. Chitosan sponge (CS, obtained by dissolution with TA-NH$_3^+$), and chitosan compounded with gelatin and sodium hyaluronate without Ag NPs (CGSH, chitosan was dissolved with TA-NH$_3^+$; CGSH-A, chitosan was dissolved with acetic acid) were prepared at the same ratio using the same method as that used for controls.

### In vitro blood clotting assay

The blood-clotting index (BCI) method described by Zhao et al. (2018), was employed to evaluate the capacity of inducing blood clot with the hemostatic material containing varying amounts of Ag NPs. Sterilized and dried samples were cut into cubes

$(0.5 \times 0.5 \times 0.5 \text{ cm}^3)$ and placed in a beaker at 37 °C in a water bath for 5 min. Hundred microliters of anticoagulant blood was dropped on the surface of the sample, followed by the addition of 20 μL 0.2 mol/L $CaCl_2$ solution. The samples were incubated at 37 °C for 5 min, after which 25 mL deionized water was added, stirred at 50 rpm and incubated at 37 °C for another 5 min. The supernatant containing blood cells, which seceded from the samples was collected and quantified at 545 nm using an UV spectrophotometer. The absorbance of citrated whole blood dispersed in deionized water was used as the reference. CGSH-A was carried out as control. All samples were evaluated three times and the BCI was calculated using the followed equation:

$$BCI = \frac{A_{545(sample)}}{A_{545(reference)}} \times 100$$

### Characterization of CGSH/Ag hemostatic material

An UV–Vis spectrophotometer (TU-1901, Beijing, China) was used to measure the absorbance of Ag NPs in CGSH/Ag hydrogels using the UV spectrum. High definition morphology of Ag NPs in CGSH/Ag hydrogels was captured using a transmission electron microscope (TEM, Tokyo, Japan). The size distribution of Ag NPs, and the zeta potential of the hemostatic material was recorded using a Zetasizer-Nano Instrument (Malvern Ltd., Tokyo, Japan). Scanning electron microscopy (SEM) and energy-dispersive X-ray spectroscopy (EDS) were performed on a scanning electron microscope (FEI, Hong Kong) to analyze the surface structure of the composites. X-ray diffraction (XRD) and X-ray photoelectron spectroscopy (XPS) methods were carried out using a diffractometer (Shimadzu XRD6000) and X-ray photoelectron spectrometer (Shimadzu, Japan), respectively. An alpha Fourier transform infrared (FTIR; Karlsruhe, Germany) analysis was performed at room temperature to determine the chemical bonds in the CGSH/Ag hemostatic material.

### Mechanical property

The mechanical property was determined with a tensile tester (Shimadzu Autograph AGS-X, Kyoto, Japan). Samples were cut into cubes ($40 \times 6 \times 2$ mm) prior to testing at a constant tension rate of 10 mm/min. Each sample was tested triply to reduce errors.

### Porosity and fluid absorption

Liquid displacement method was used to determine the porosity of the hemostatic material. Cubic shaped samples ($10 \times 10 \times 10$ mm$^3$) were dried, weighed ($W_0$), and immersed in 20 mL (V) ethanol at 37 °C for 24 h to ensure the pores of the samples were saturated. The samples were hung in the air for 30 s, and weighed ($W_t$). Three times of the same measurement were performed. Porosity was calculated using the following equation:

$$\text{Porosity } (\%) = \left( \frac{W_t - W_o}{\rho_{ethanol}} \times \frac{1}{V} \right) \times 100$$

The fluid absorption of the samples was determined by assessing the weight changes before and after absorption of PBS (pH 7.4) and anticoagulant blood. Dried samples with the same weight ($W_d$) were immersed in PBS or blood, and incubated at 37 °C for 10 min. After retrieving the samples, the fluid on the surface was removed using a filter paper to measure the wet weight ($W_w$). Three measurements were performed for each sample. Liquid absorption ratio was determined using the following equation:

$$\text{Fluid absorption ratio } (\%) = \frac{W_w - W_d}{W_d} \times 100$$

### Platelet adhesion study

PRP was used for the platelet adhesion tests. Sterile samples were cut into small pieces of $1 \times 1$ cm$^2$ with 0.25 cm thickness. The samples were immersed in 10 mL of PBS and incubated at 37 °C for 30 min, following which 0.5 mL PRP was added and incubated at 37 °C for another 30 min. PBS was used to wash the material three times to wipe off nomadic platelets. The adhered platelets on the surface were treated with 0.25 mL 1% Triton X-100 in PBS, and a kit (Sigma-Aldrich, St. Louis, MO, USA) was used to measure the lactate dehydrogenase (LDH) activity. The number of platelets captured by the sample was measured by determining their absorbance at 490 nm, and the same sample was tested three times. Additionally, the samples were fixed with 2.5% glutaraldehyde, and dehydrated consequently with 50, 60, 70, 80, 90, and 100% ethanol

for 10 min. After the material dried naturally, the morphology of the adhered platelets was observed using a scanning electron microscope.

In vitro degradation study

The degradability in vitro of CS, CGSH, CGSH/Ag40, CGSH/Ag50, and CGSH/Ag60 were determined by calculating the residual ratio of weight after immersing them in the simulated body fluid (SBF, pH 7.4). Briefly, 0.5 g of the sample ($W_o$) was mixed with 20 mL of SBF and then cultured on an orbital shaker at 37 °C. The SBF was replaced daily. The sample residuals were then separated from the SBF solution by filtration at the specific day (1st, 2nd, …, 10th day), and dried at 60 °C to obtain a constant weight ($W_a$). The residual ratio of weight was calculated according to equation:

$$Residue\ ratio\ (\%) = \left(\frac{W_a}{W_o}\right) \times 100$$

In vitro hemolysis test

The hemolysis ratios of CGSH/Ag40, CGSH/Ag50, and CGSH/Ag60 were evaluated in vitro. 5 mL anticoagulated rabbit blood (containing 0.38% sodium citrate) was mixed with 10 mL of PBS (pH 7.4), and centrifuged at 1200 rpm for 5 min to collect red blood cells (RBCs). 60 μL RBC dispersion was added to 3 mL of 1 mg/mL sample suspension and cultured at 37 °C for 1 h. Centrifugation at 2000 rpm for 5 min was performed to obtain supernatant, the absorbance at 545 nm was recorded. Distilled water and PBS without sample were used as the positive control and negative control, respectively. The hemolytic rate (H) was determined using equation:

$$H(\%) = \left(\frac{D_s - D_p}{D_d - D_p}\right) \times 100\%$$

where $D_s$, $D_p$, and $D_d$ are the absorbance values of the sample, PBS, and distilled water, respectively.

Cytotoxicity and cell adhesive behavior tests

L929 mouse skin fibroblasts were used to assess the cytotoxicity of the composites with the 3-(4,5-dimethylthiazol-2-yl)-2,5-diphenyltetrazolium (MTT) assay. The UV-sterilized samples of CGSH/Ag40, CGSH/Ag50, and CGSH/Ag60 were cultured with 1 mL sterile Dulbecco's Modified Eagle's Medium (DMEM) for 72 h at 37 °C. The leaching liquid was collected from dissolved samples. The L929 cells were seeded in a 96-well plate ($3 \times 10^5$ cells/well), to which 100 μL DMEM containing 10% fetal bovine serum and 50 μL aliquot of the leached liquid was added, and cultured at 37 °C. After incubation for 24, 48, or 72 h, 10 μL of MTT solution was added to the medium and incubated for 4 h. Finally, 10 μL dimethyl sulfoxide (DMSO) was added to dissolve the formazan crystals. To assess cell viability, absorbance at 490 nm was measured using a microplate reader (iMark, CA, USA).

Live and dead L929 cells incubated with CGSH/Ag40, CGSH/Ag50, and CGSH/Ag60 for 24 h were differentiated using light and fluorescence microscopes (Nikon TS 100, Japan) after staining with calcein-AM and propidium iodide (PI).

The cell adhesion was evaluated using the previously reported method (Li et al. 2017a; Zhang et al. 2019). The $1 \times 10^4$ L929 cells were seeded onto CGSH/Ag40, CGSH/Ag50, CGSH/Ag60, and the blank culture plate (used as the control), prior to culturing for 24 h. Following fixation with 4% paraformaldehyde, and staining with calcein-AM and propidium iodide (PI), the adhered cells were then observed with a confocal microscope (Zeiss, LSM710, Germany) to obtain their morphology.

Antimicrobial assessment

Antimicrobial activity was tested using the inhibition zone method. Bacterial suspension of *Staphylococcus aureus* or *Escherichia coli* ($10^7$ CFU/mL) were spread on agar medium, and sterilized dry composite samples (discs, 17 mm in diameter) were placed on the medium. These plates were incubated at 37 °C for 12 h, after which the size of the inhibition zones was recorded. The CGSH/Ag samples incubated with bacteria were used for SEM observation.

Activated partial thromboplastin time (APTT) and pro-thrombin time (PT) analysis

An automated coagulation analyzer (Sysmex CA-1500, Tokyo, Japan) was used to evaluate APTT and PT. PPP and APTT agent were mixed and cultured at 37 °C for 5 min, following which the sample and 100 μL of 0.2 mol/L $CaCl_2$ solution were added. The

clotting time was measured as APTT. For PT calculation, PPP was mixed with PT solution and incubated at 37 °C for 5 min, after which sample and 100 µL of 0.2 mol/L CaCl$_2$ solution were added, and the PT was recorded. All samples were evaluated three times.

## In vivo hemostasis study

Rabbits used for ear artery and liver bleeding models were anesthetized and tied to operating table with gauze. The hair on ears or abdomen was shaved and the exposed skin was disinfected with tincture of iodine. For ear artery bleeding model, a wound approximately 1 cm long was made on the ear using a scalpel to cut the artery. In the liver artery bleeding model, a crosswise wound 0.5 cm deep and 1 cm long was created on the liver. After free bleeding for 5 s, the ultraviolet sterilized samples (2 cm in diameter and 0.5 cm in height) were placed on the wound with gentle pressing. The bleeding time was measured, and the wounds were photographed. Each sample was tested six times in each model. After surgery, the rabbits were cared for and observed in divided cages.

## Wound healing and histological evaluation

After anesthetization, shaving and disinfection, five full-thickness wounds (each 2 cm in diameter) were made on the rabbit's back. The five wounds on each rabbit were divided into blank, CS, CGSH, CGSH/Ag50, and Mepitel® groups ($n = 6$). The samples with the same shape and size as the wounds were ultraviolet sterilized and placed on the wounds with adhesive bandage to fix the wound dressing. After careful caging for 3, 7, 11, and 14 days, the rabbits were euthanized, and the wounds were photographed to assess the wound contraction ratio. The muscle and skin around the wounds were excised, fixed in 10% buffered formalin, embedded in paraffin and sectioned vertically. The sections were stained with hematoxylin and eosin (H&E) and examined using light microscopy.

## Results and discussion

### Blood coagulation in vitro

BCI was determined to assess the blood coagulation effects of CGSH/Ag composites with various dosages of Ag NPs. A low BCI value indicates stronger capacity of the hemostatic material to induce thrombosis in blood. As Fig. 1a shows, the BCI value of CGSH was lower than that of CGSH-A, indicated the better ability to clot blood of CGSH, can be due to the blood clotting function of TA-NH$_2$, which was formed from TA-NH$_3^+$ after the dissolution of chitosan in preparation. samples containing different doses of Ag NPs resulted in varying degrees of induction of blood coagulation. With increasing the Ag NO$_3$ dosage from 0 to 40 µg/g in the preparation, the BCI of the CGSH/Ag composites continuously decreased, and was $52 \pm 2.1$, $32 \pm 2.6$, $27 \pm 2.4$, $22 \pm 2.3$, and $20 \pm 2.5$ for 0, 10, 20, 30, and 40 µg/g of Ag NO$_3$, respectively. When the Ag NO$_3$ concentration in the preparation reached 50 µg/g, the BCI was $19 \pm 0.7$. The BCI of CGSH/Ag composites prepared with 60, 70, 80, 90, 100, 200, and 300 µg/g Ag NO$_3$ were $20 \pm 0.6$, $22 \pm 2.4$, $30 \pm 2.5$, $37 \pm 0.8$, $41 \pm 0.5$, $56 \pm 2.5$, and $58 \pm 2.7$, respectively. Thus, the composite with the best thrombogenic activity was prepared by using 50 µg/g Ag NO$_3$ (CGSH/Ag50), which was chosen for all characterizations, and composites prepared with 40 and 60 µg/mL Ag NO$_3$ (CGSH/Ag40 and CGSH/Ag60, respectively) were used as controls.

### Characterization of CGSH/Ag composites

As shown in Fig. 1b, the Ag NPs in CGSH/Ag composites obtained by using gelatin as reducer and protective agent were characterized using TEM. The average sizes of $6.8 \pm 0.56$, $7.2 \pm 0.24$, and $8.3 \pm 0.68$ nm were observed for Ag NPs in CGSH/Ag40, CGSH/Ag50, and CGSH/Ag60, respectively. Their respective space lattices were 0.236, 0.233, and 0.232 nm, which is similar to the (111) lattice spacing of Ag NPs (0.236 nm) (Zeng et al. 2015). Figure 1c shows the UV spectra, and the absorbance peaks for CGSH/Ag40, CGSH/Ag50, and CGSH/Ag60 hydrogel were around 400 nm with a slight blue shift, which increased with the dosage of Ag NO$_3$. The blue shift and corresponding intensity increased with increasing the dosage of AgNO$_3$. Additionally, the solutions of Ag NPs under sunlight showed various degrees of yellow color, with the color intensifying with the increasing Ag NO$_3$ dosage. These results suggest that upon increasing the Ag NO$_3$ content, the NP size
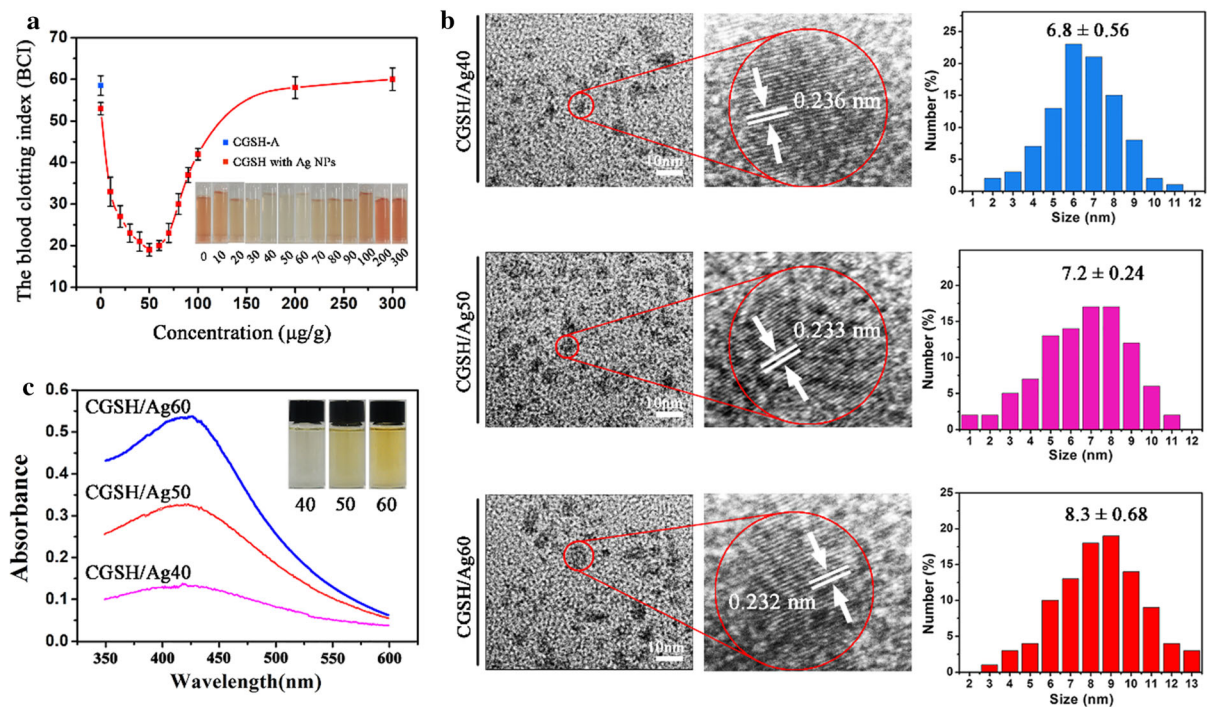
Fig. 1 a Different BCI values induced by CGSH/Ag composites with different Ag NO₃ dosage, and the corresponding images are shown, where darker red color indicates lower blood coagulation capacity. b TEM images of Ag NPs in CGSH/Ag40, CGSH/Ag50, and CGSH/Ag60 hydrogel, and their corresponding size-distributions. c UV spectra of the obtained CGSH/Ag40 (40), CGSH/Ag50 (50), and CGSH/Ag60 hydrogels; inserts show the corresponding images

increases and results in a higher absorbance peak around 400 nm.

In order to thoroughly investigate the morphology changes of the obtained composites, the surface morphology of samples was observed using SEM. As Fig. 2a shows, in the surface structure of CS, wild tablets without regulation can be observed. The CGSH displays regular and stratified porous structure, while CGSH/Ag40, CGSH/Ag50, and CGSH/Ag60 show more regular and homogeneous porous structure. The rich, regular, and symmetrical porous structure could absorb blood and exudate on wounds to promote hemostasis and wound healing. The EDS mapping presented in Fig. 2b shows the distribution of the main elements C, O, N, and Ag in CGSH/Ag50, and confirms the uniform distribution of Ag NPs in CGSH/Ag50.

Figure 2c shows the FTIR spectra of CS, CGSH, CGSH/Ag40, CGSH/Ag50, and CGSH/Ag60. The peak observed at 3425 cm$^{-1}$ was ascribed to the hydrogen bond stretching vibration of –OH, and the peaks around 2921 cm$^{-1}$ and 2887 cm$^{-1}$ were ascribed to the C–H of methylene and methyl, respectively. The carbonyl stretching –C = O and

deformation vibration N–H (amide I, amide II bands) could also be observed from 1653 to 1603 cm$^{-1}$. The peak at 1083 cm$^{-1}$ was attributed to the vibration of C–O–C. The five spectra show similar peaks that could be due to chitosan, the main ingredient in these composites. These results suggest that the existence of Ag NPs induces negligible impact on the structure of CGSH, which acts as a scaffold for supporting the Ag NPs (Ye et al. 2016).

The XRD patterns of CS, CGSH, CGSH/Ag40, CGSH/Ag50, and CGSH/Ag60 are presented in Fig. 2d. The main diffraction characteristics of CS and CGSH were similar, but different from those of CGSH/Ag40, CGSH/Ag50, and CGSH/Ag60. The spectra of CGSH/Ag40, CGSH/Ag50, and CGSH/Ag60 showed peaks at 38.2 and 44.2°, which were assigned to (111) and (200) planes, respectively. The intensity of the two peaks at 38.2 and 44.2° increased with the rise in Ag NPs dosage in the CGSH/Ag composites. Additionally, Ag NPs resulted in unobvious changes on the crystals of CGSH/Ag40, CGSH/Ag50, and CGSH/Ag60 compared to CGSH and CS, which may be due to the weak dosage.
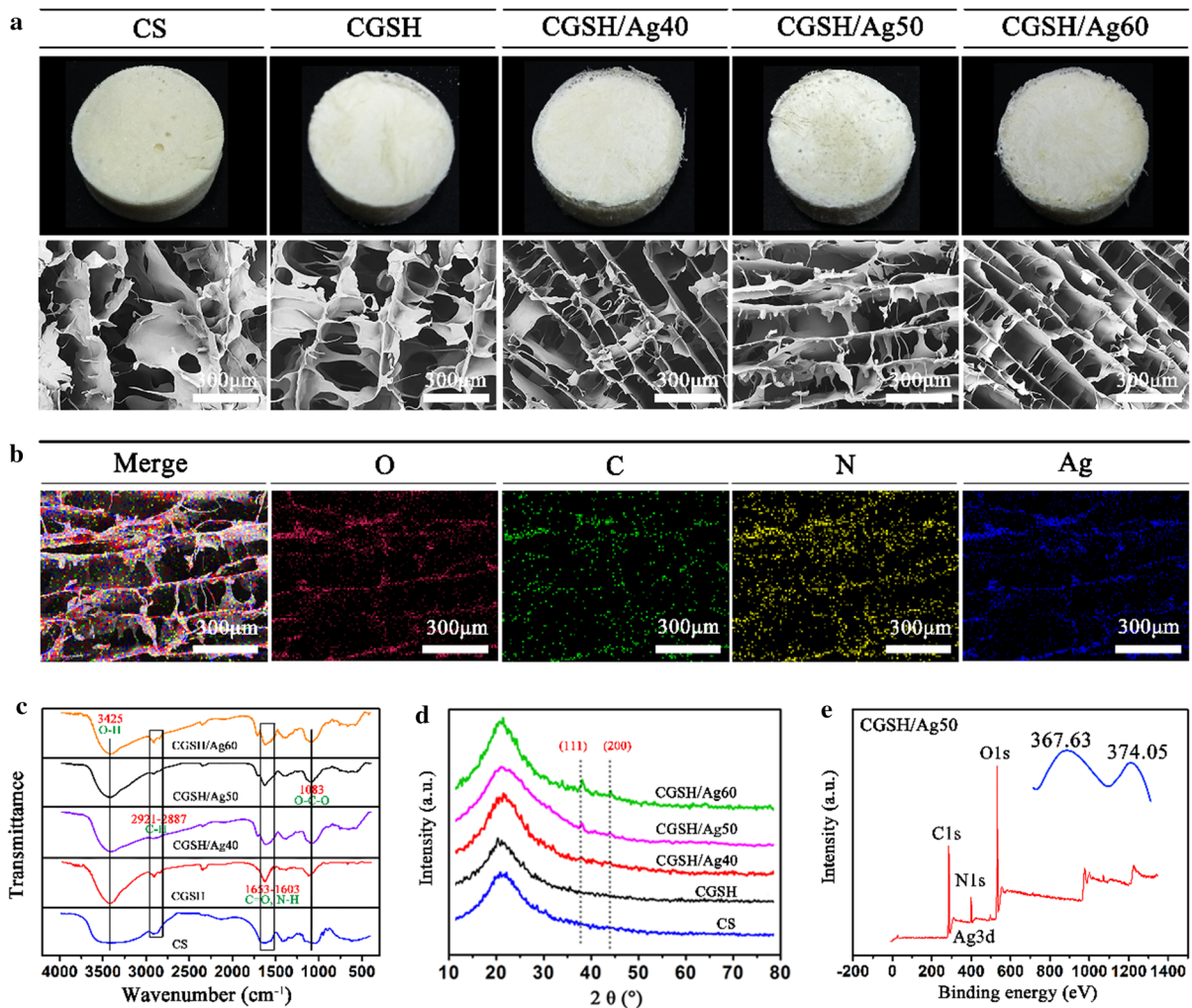
**Fig. 2** **a** Photographs and SEM images of the composite surface. **b** EDS mapping images of CGSH/Ag50. **c** FTIR spectra, **d** XRD spectra, and **e** XPS spectrum

Figure 2e shows the XPS full scanned spectra of CGSH/Ag50. The peaks at 291.8, 400.4, and 537.6 eV were assigned to the C1 s, N1 s, and O1 s from the composite, respectively. The peaks at 367.6 and 374.5 eV were contributed by Ag 3d. These data convincingly demonstrate that the Ag NPs have been stably immobilized by hydrogen bond and Vander Waals forces because of the –NH$_2$ and –OH groups (Ye et al. 2016).

## Mechanical property, porosity and liquid absorption ratio study

The mechanical properties of CS, CGSH, CGSH/Ag40, CGSH/Ag50, and CGSH/Ag60 are shown in Fig. 3a. CS and CGSH showed relatively lower stress at the breaking point at 0.72 and 0.78 MPa, respectively. After composited with Ag NPs, the stress slightly increased to 0.82, 0.85, and 0.86 MPa for CGSH/Ag40, CGSH/Ag50, and CGSH/Ag60, respectively, suggesting that the CGSH/Ag50 has potentials as a wound dressing with enhanced mechanical strength.

The porosity and liquid absorbing properties of the composites were evaluated. As Fig. 3b shows, the porosity of CS, CGSH, CGSH/Ag40, CGSH/Ag50, and CGSH/Ag60 were 53 ± 2.3, 67 ± 1.5, 72 ± 1.6, 71 ± 2.6, and 71 ± 1.8%, respectively. The high porosity of CGSH compared to CS may be because of the compounding of chitosan, gelatin, and sodium
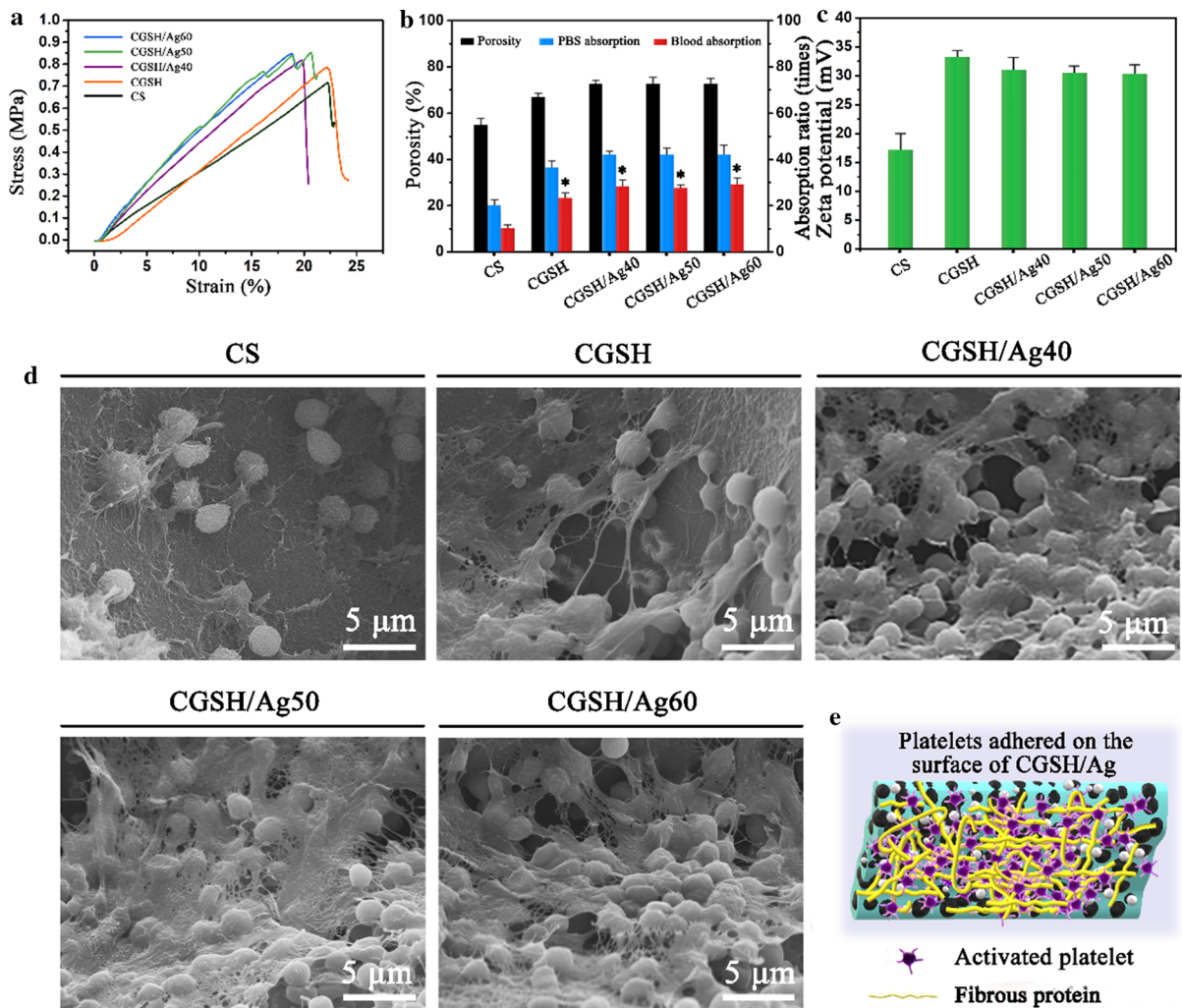
Fig. 3 **a** Mechanical behavior. **b** Porosity and absorption ratio measurement for PBS and blood. **c** Zeta potential evaluation. **d** SEM images of platelet adhesion on the surface of composites CS, CGSH, CGSH/Ag40, CGSH/Ag50, and CGSH/Ag60. **e** Conceptional illustration of platelet aggregation on the surface of CGSH/Ag composites. * Indicates $P < 0.05$

hyaluronate. The higher porosity of CGSH/Ag40, CGSH/Ag50, and CGSH/Ag60 compared to CGSH could be explained by the regular porous structure. The PBS absorption ratios of CS, CGSH, CGSH/Ag40, CGSH/Ag50, and CGSH/Ag60 were $19 \pm 2.1$, $28 \pm 2.4$, $42 \pm 1.6$, $41 \pm 1.8$, and $41 \pm 2.5$-fold higher than their primary weights, respectively. Moreover, CGSH, CGSH/Ag40, CGSH/Ag50, and CGSH/Ag60 could absorb approximately 20-times more blood than their initial weights, which is much higher than that of CS ($9 \pm 1.5$-times). This eminent PBS and blood uptake property may be because of the existence of –OH and –NH₂, and a rich porous structure in these hydrogels (Kovach et al. 2016).

Thus, the high blood absorption ability endowed CGSH/Ag50 with fundamental potential as hemostatic material.

Zeta potential

Chitosan has been widely researched as a hemostatic material because of its positively charged surface, which can promote platelet aggregation by potential stimulation. The zeta potential of the composites was determined and is shown in Fig. 3c. The zeta potential of CS was $16.3 \pm 2.2$ mV, which can be explained by the $-NH_3^+$ from chitosan (Shimojo et al. 2016). CGSH showed a high zeta potential of $33.5 \pm 1.4$ mV, and

the existence of Ag NPs decreased the positive zeta potential to $31.2 \pm 2.6$, $30.6 \pm 1.3$, and $30.3 \pm 1.7$ mV for CGSH/Ag40, CGSH/Ag50, and CGSH/Ag60, respectively. This result suggests that gelatin enhances the positive potential in CGSH, most likely through the number of positive charge fragments (such as $-NH_3^+$). While Ag NPs can compound with the $-NH_3^+$ of gelatin in CGSH/Ag40, CGSH/Ag50, and CGSH/Ag60, and decrease their positive potential (Pourjavadi and Soleyman 2011). The enhanced positive zeta potential of CGSH/Ag50 can be useful in inducing platelet activation and aggregation, which can contribute to controlling hemorrhage (Feng et al. 2016).

Observation of adhering platelets

Platelet aggregation and activation is vital for hemostatic material to promote blood clots and block bleeding in hemostasis (Li et al. 2017a). The platelet adhesion on the surface of hemostatic material was viewed to assess platelet aggregation. After contact with platelets, CS, CGSH, CGSH/Ag40, CGSH/Ag50, and CGSH/Ag60 capture varying number of platelets on their surface (Fig. 3d). CS induced very little

platelet aggregation with minor fibrin protein formation, which can be related to the positive potential charge (Hattori and Ishihara 2017). The increased aggregation of platelets with fibrin protein was observed for CGSH, which may be due to its enhanced positive potential. A large number of platelets wrapped with webbed fibrin were observed on the surface of CGSH/Ag40, CGSH/Ag50, and CGSH/Ag60. The agglomerated hemostatic ingredients could act as a plug to block the damaged blood vessels in controlling hemorrhage (Fig. 3d). This result corresponds to the number of platelets adhered onto the composite surface. CGSH/Ag40, CGSH/Ag50, and CGSH/Ag60 captured more platelets than CS and CGSH (Fig. 4a). The capacity of CGSH/Ag40, CGSH/Ag50, and CGSH/Ag60 in inducing platelet aggregation could be because of the effects of Ag NPs, which promote phosphatidylserine exposure and thrombin generation (Jun et al. 2011).

It is worth noting that there were differences in the number of platelets adhered on the surface of CGSH/Ag40, CGSH/Ag50, and CGSH/Ag60. CGSH/Ag50 captured more platelets on its surface than CGSH/Ag40, which directly correlates to the higher dosage of settled Ag NPs that can induce more platelet



Fig. 4 a The number of platelets adhered on the surface of composites CS, CGSH, CGSH/Ag40, CGSH/Ag50, and CGSH/Ag60. b Weight residue ratios. c Hemolysis assay. d L929 cell viability assays. * Indicates $P < 0.05$
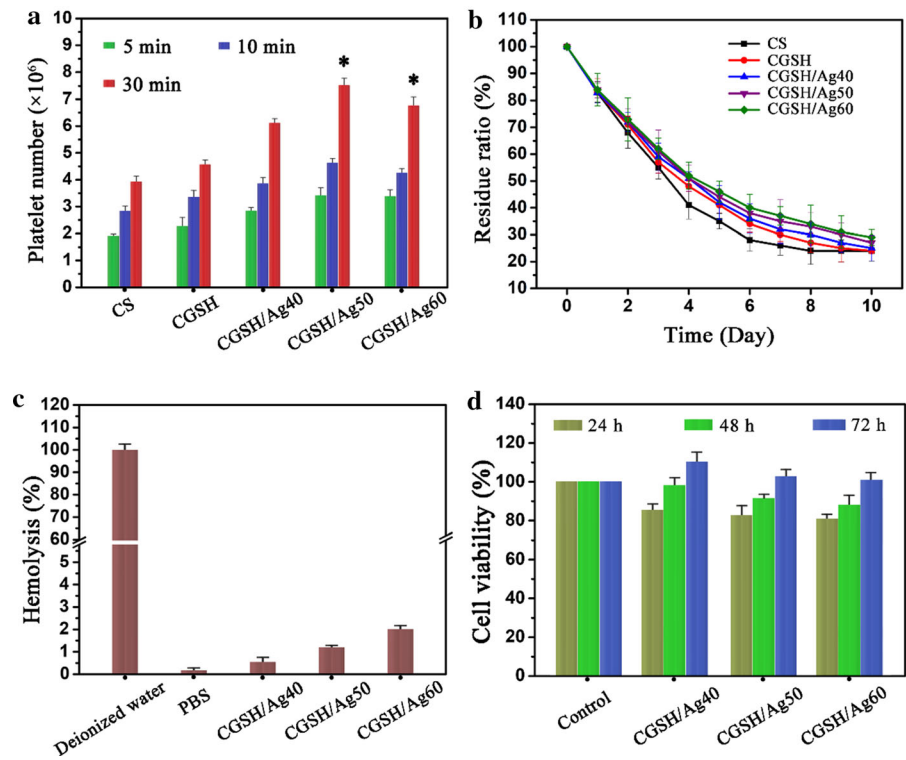
aggregation. However, CGSH/Ag60 with higher Ag NPs showed lower platelet aggregation than CGSH/Ag50. We speculate that with increasing Ag NPs dosage in CGSH/Ag, there is a detrimental effect of Ag NPs on platelets, which may result in the loss of their ability to aggregate and activate.

In vitro degradation, hemolysis and cytotoxicity assay

The residual ratios of weight for CS, CGSH, CGSH/Ag40, CGSH/Ag50, and CGSH/Ag60 were determined to evaluate in vitro degradability (Fig. 4b). Samples were degraded progressively with increased time in general. Among them, the composites containing Ag NPs showed decreased degradation rate when compared with CS and CGSH. On the 10th day, the residual ratios of CGSH/Ag50 was about 28%, which were minimally higher that of CS and CGSH (about 25%), suggesting the good biodegradation property of CGSH/Ag50 as a safe wound dressing.

Hemolysis by the hemostatic material was evaluated to study the effect of CGSH/Ag50 on

erythrocytes. As Fig. 4c shows, all the hemostatic materials exhibited low hemolysis ratio, under 5%, suggesting good blood compatibility (Long et al. 2017). Additionally, an increase in the hemolysis ratio was observed with increasing Ag NPs dosage in the composites, which were $0.5 \pm 0.8$, $1.2 \pm 0.6$, and $2 \pm 0.7\%$ for CGSH/Ag40, CGSH/Ag50, and CGSH/Ag60, respectively.

The cytotoxicity associated with the three composites was evaluated using L929 cells. For all time points tested, the L929 cells showed cell viability above 80% after incubation with CGSH/Ag40, CGSH/Ag50, and CGSH/Ag60 for 1 day (Fig. 4d). The cell viability was higher and over 100% for all composites after culturing for 3 days, suggesting that the composites display no cytotoxicity towards L929 cells. The cell viability of composite containing high dosage of Ag NPs was lower than cell viability of composite with low dosage of Ag NPs, which corresponds to the fluorescence and light microscope images obtained after treatment for 1 day. Live cells that adhere to the bottom of the culture dish are stained green, and the cells treated with CGSH/Ag40 showed more live cells
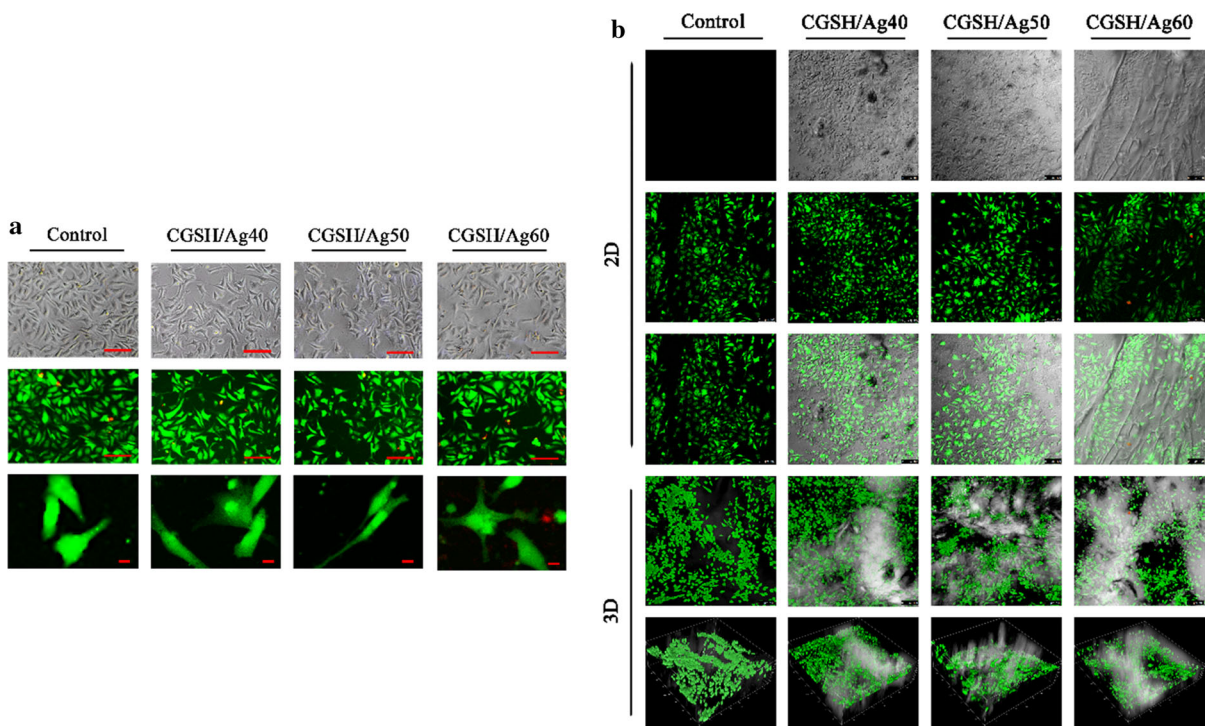


Fig. 5 a Bright and fluorescence images of L929 cells in control, CGSH/Ag40, CGSH/Ag50, and CGSH/Ag60 groups after culturing for 24 h (scale bar = 50 μm); the high-definition

fluorescence images showed the morphology of cells (scale bar = 5 μm). b Morphology of L929 cells grown on the samples

than CGSH/Ag50 and CGSH/Ag60 (Fig. 5a). Accordingly, more red-stained dead cells could be viewed floating in the solution in CGSH/Ag60 group than in the CGSH/Ag40 and CGSH/Ag50 groups. Furthermore, it was observed that the attached cells maintained their normal, tridimensional, and fusiform morphology on these composites, suggesting no obvious adverse impacts of CGSH/Ag50 on the growth of cells (Fig. 5b).

Taken together, these results suggest that CGSH/Ag composites can promote more platelet aggregation than CS and CGSH, owing to the aggregation and activation property of Ag NPs. In addition, they do not cause cytotoxicity. With the increase in Ag NPs dosage in these composites, the aggregation of platelets enhanced. However, when the Ag $NO_3$ dosage in preparation was above 50 μg/mL, the aggregation of platelets decreased. The results of hemolysis and L929 cell cytotoxicity assays showed that upon increasing the Ag $NO_3$ dosage in the preparation, the toxicity of CGSH/Ag composites increased. When the Ag $NO_3$ dosage in preparation was above 50 μg/mL, the aggregation of platelets decreased, which may be the result of detrimental effects of Ag NPs on platelets that the devitalized platelets no longer aggregate on the surface of CGSH/Ag composites.

APTT and PT measurements

APTT and PT were investigated to assess the intrinsic and extrinsic coagulation pathway, respectively, of CGSH/Ag composites. As shown in Fig. 6a, APTT was reduced by the CGSH/Ag composites compared to CS and CGSH. However, no significant changes in PT was observed, suggesting that the composites exhibit no obvious effect. Based on these observations, CGSH/Ag40, CGSH/Ag50, and CGSH/Ag60 exhibit intrinsic blood coagulation capacity (Feng et al. 2016).

Antibacterial activity testing

CS and CGSH showed unconspicuous bacterial inhibition zone, indicating their weak antibacterial activity against *E. coli* and *S. aureus* (Fig. 6b). The result appears not in line with the reported studies (Cai et al. 2016, 2018). This can be ascribed to the lower degree of acetylation of chitosan (85%) used in the present study for preparation of CS and CGSH, as it has been proved previously that lower degree of acetylation of chitosan led to poorer antibacterial activity (Mishra et al. 2016; Younes et al. 2014). On the other hand, CGSH/Ag40, CGSH/Ag50, and CGSH/Ag60 exhibited efficient antibacterial activity, with inhibition



Fig. 6 **a** APTT and PT measurements. **b** Agar plates showing inhibition zones against *E. coli* and *S. aureus*. **c** The average size of the inhibition zones for composites CS, CGSH, CGSH/Ag40, CGSH/Ag50, and CGSH/Ag60. **d** SEM images of *E. coli* and *S. aureus* obtained before and after inhibition with CGSH/Ag50. * Indicates $P < 0.05$
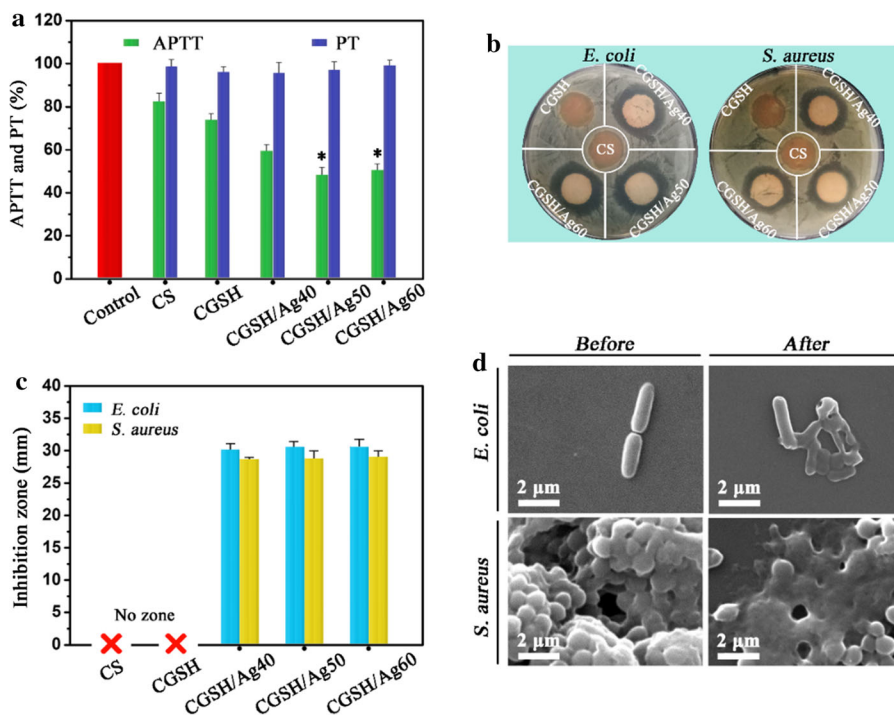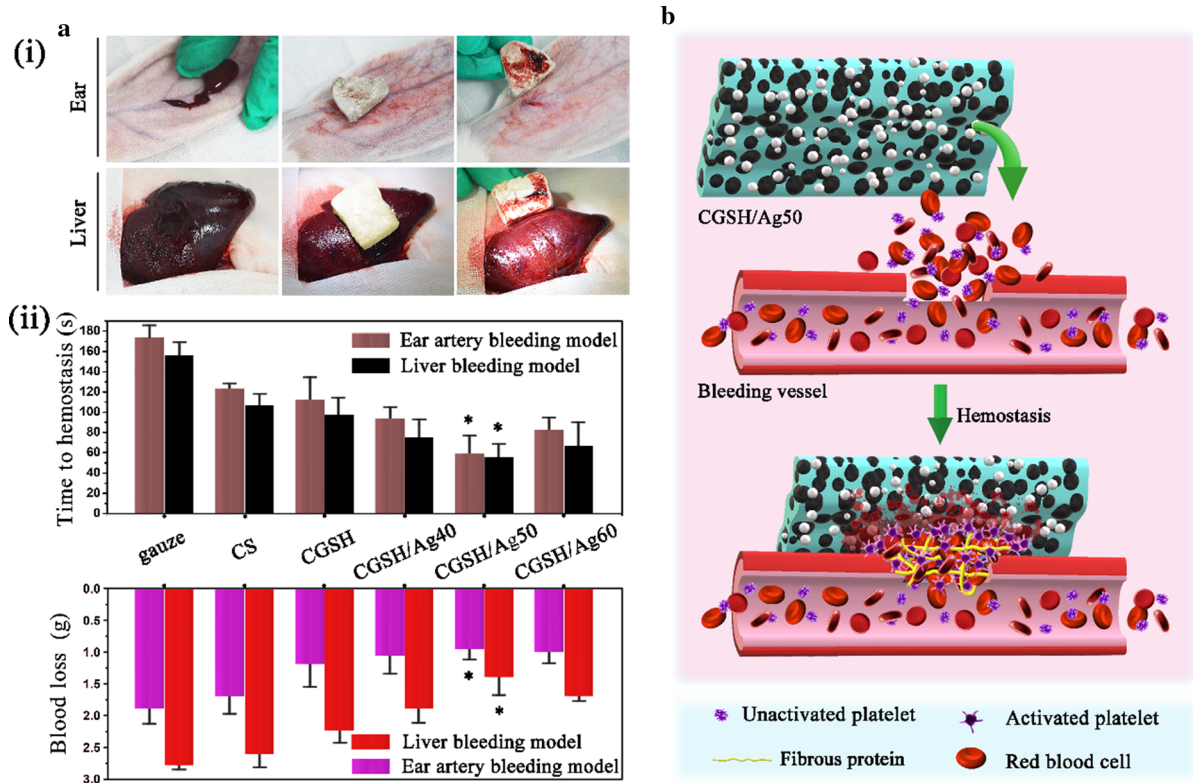
**Fig. 7 a** Images of controlling hemorrhage, (i) application of CGSH/Ag50 in rabbit ear and liver bleeding models, (ii) Time to hemostasis of CS, CGSH, CGSH/Ag40, CGSH/Ag50, and CGSH/Ag60 in rabbit ear and liver bleeding models, and their corresponding blood loss weight. **b** Conceptual representation of CGSH/Ag50 controlling hemorrhage. After being applied to the wound, a hemostatic plug containing platelets, erythrocytes, and fibrin protein is formed to block the wound and stop bleeding. * Indicates $P < 0.05$

zone sizes of approximately 30 mm against *E. coli* and 27 mm against *S. aureus* (Fig. 6c). No differences in the antibacterial activities between CGSH/Ag40, CGSH/Ag50, and CGSH/Ag were observed may because of their nearly Ag NPs dosage. SEM analysis of the morphology changes in *E. coli* and *S. aureus* before and after incubation with CGSH/Ag50 showed that the bacteria were plump with integrated cell membrane before culturing with composite, but not after (Fig. 6d). This observation suggests good antibacterial activity of CGSH/Ag50, which makes it a good hemostatic material with the capacity to prevent bacterial infection after hemostatic surgery.

Hemostasis assay in vivo

Rabbit bleeding models were employed to assess the hemostasis capacity of the composites in vivo. In the ear artery bleeding model, CS, CGSH, CGSH/Ag40,

CGSH/Ag50, and CGSH/Ag60 successfully controlled bleeding in $124.3 \pm 3.3$, $111.5 \pm 19.5$, $92.3 \pm 8.6$, $57.2 \pm 17.2$, and $82.3 \pm 8.1$ s, respectively (Fig. 7a). And after hemostasis, their blood loss weight was $1.62 \pm 0.31$, $1.23 \pm 0.44$, $1.1 \pm 0.26$, $0.97 \pm 0.11$, and $1.08 \pm 0.15$ g, respectively. The time to hemostasis of the composites was shorter in the liver bleeding model, but the corresponding blood loss weight was higher. CS, CGSH, CGSH/Ag40, CGSH/Ag50, and CGSH/Ag60 stopped liver bleeding in $107.3 \pm 11.6$, $94 \pm 13.6$, $71 \pm 14.2$, $53.6 \pm 11.7$, and $62.4 \pm 21.3$ s, respectively, and the respective blood loss weight was $2.7 \pm 0.33$, $2.3 \pm 0.24$, $1.75 \pm 0.23$, $1.47 \pm 0.35$, and $1.54 \pm 0.09$ g. These results confirm the excellent hemostatic ability of CGSH/Ag50. The hemostasis mechanism of CGSH/Ag50 can be attributed to the excellent blood uptake property, activation of positively charged surface on platelets, and the activation of Ag NPs on platelets. In
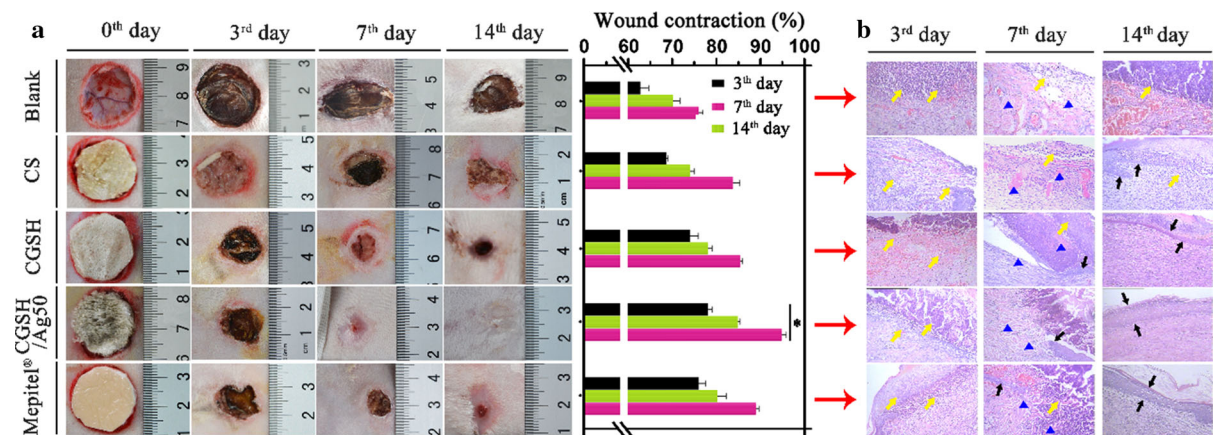
**Fig. 8** **a** Images of wound healing and the corresponding wound contractions. * Indicates $P < 0.05$. **b** Histological analysis. Yellow arrows show edema and inflammatory cells. Blue triangles and black arrows refer to granulation and skin, respectively

the progress of hemostasis, when CGSH/Ag50 is applied to the bleeding wound, it absorbs and holds the gushing blood through the activation of positively charged surface and Ag NPs (Fig. 7b). CGSH/Ag50 can aggregate and activate platelets on the surface of the composite together with fibrin formation (as shown in Fig. 3d), which promotes blood clotting and serves as a hemostatic plug to block the wounded vessel. Thus, the hemorrhage can be successfully controlled in a short time by CGSH/Ag50.

Wound healing study

The application of CGSH/Ag50 in wound healing was studied in full-thickness wound models. As Fig. 8a shows, CGSH/Ag50 acts as a wound dressing in good capacity and promotes wound healing. On the 3rd and 7th day, wounds treated with CS, CGSH, Mepitel®, and untreated wounds remained as variform scabs, while the wounds treated with CGSH/Ag50 only had light scars. After 14 days, the wounds treated with CGSH/Ag50 had nearly completely healed, and wound contraction was approximately $94 \pm 2.8\%$, which was higher than CS ($73 \pm 3.2\%$), CGSH ($77 \pm 3.1\%$), Mepitel® ($83 \pm 1.5\%$), and control ($60 \pm 2.4\%$) groups. Furthermore, compared to a recently reported hydrogel wound dressing (Li et al. 2018) that spent 3 weeks for wound healing, the CGSH/Ag50 prepared in the present study required only 2 weeks, demonstrating its excellent capacity in wound healing.

The histological analysis showed edema and inflammatory cells in the control, CS, CGSH,

CGSH/Ag50, and Mepitel® groups on the 3rd day (Fig. 8b). On the 7th day, granulation was observed in all the groups, while edema and inflammatory cells still existed in the control, CS, and CGSH groups. In the Mepitel® group, edema and inflammatory cells were reduced, and in the CGSH/Ag50 group no edema or inflammatory cells were observed and new skin appeared. On the 14th day, complete as well as thin skin was observed in the CGSH and Mepitel® groups, while in the CGSH/Ag50 group, complete, thick, and even skin had formed. No complete skin was observed in the control, CS, and CGSH groups. The full-thickness wound models and histological analysis show that CGSH/Ag50 can significantly promote wound healing, owing to its good exudate uptake property, biocompatibility, and excellent antibacterial activity.

**Conclusion**

Chitosan/gelatin/sodium hyaluronate hemostatic dressing based on silver nanoparticles was successfully prepared and characterized. The composite CGSH/Ag50 showed high porosity and absorbed large amounts of blood. Owing to its ability of stimulating from positively charged surface and Ag NPs, the platelets were activated and aggregated on the surface of CGSH/Ag50 to block wound bleeding for hemostasis. In the hemolysis and L929 cell cytotoxicity assays, CGSH/Ag50 exhibited good hemocompatibility and cytocompatibility. In rabbit bleeding models, CGSH/

Ag50 showed excellent hemostatic activity that could control hemorrhage in a short time. Additionally, CGSH/Ag exhibited good antibacterial activity against *E. coli* and *S. aureus*, and prominent capacity to promote wound healing. Thus, the efficient hemostatic activity of CGSH/Ag, together with its anti-infection and wound healing activities, highlights the potential of CGSH/Ag50 as a novel hemostatic material. However, more intricate and larger bleeding models need to be studied in the future to develop clinical applications of CGSH/Ag50 for hemorrhage control.

# References

Abdel-Rahman RM, Abdel-Mohsen AM, Hrdina R, Burgert L, Fohlerova Z, Pavliňák D, Sayed ON, Jancar J (2016) Wound dressing based on chitosan/hyaluronan/nonwoven fabrics: preparation, characterization and medical applications. Int J Biol Macromol 89:725–736

Baylis JR, Ju HY, Thomson MH, Kazerooni A, Wang X, John AES, Lim EB, Chien D, Lee A, Zhang JQ (2015) Self-propelled particles that transport cargo through flowing blood and halt hemorrhage. Sci Adv 9:e1500379–e1500379

Berce C, Muresan M-S, Soritau O, Petrushev B, Tefas L, Rigo I, Ungureanu G, Catoi C, Irimie A, Tomuleasa C (2018) Cutaneous wound healing using polymeric surgical dressings based on chitosan, sodium hyaluronate and resveratrol. A preclinical experimental study. Colloids Surf B Biointerfaces 163:155–166

Bonaventura G, Cognata V, Iemmolo R, Zimbone M, Contino A, Maccarrone G, Failla B, Barcellona ML, Francesca LC, D'Agata V (2018) Ag-NPs induce apoptosis, mitochondrial damages and MT3/OSGIN2 expression changes in an in vitro model of human dental-pulp-stem-cells-derived neurons. Neurotoxicology 67:84–93

Cai N, Li C, Han C, Luo X, Shen L, Xue Y, Yu F (2016) Tailoring mechanical and antibacterial properties of chitosan/gelatin nanofiber membranes with Fe$_3$O$_4$ nanoparticles for potential wound dressing application. Appl Surf Sci 369:492–500

Cai N, Zeng H, Fu J, Chan V, Chen M, Li H, Yu F (2018) Synergistic effect of graphene oxide-silver nanofillers on engineering performances of polyelectrolyte complex nanofiber membranes. J Appl Polym Sci 19:46238

Chang YC, Lee CJ, Wang LW, Wang YH (2018) Highly uniform resistive switching properties of solution-processed silver-embedded gelatin thin film. Small 14(13):1703888

Feng C, Li J, Wu GS, Mu YZ, Kong M, Jiang CQ, Cheng XJ, Liu Y, Chen XG (2016) Chitosan-coated diatom silica as hemostatic agent for hemorrhage control. ACS Appl Mater Interfaces 50:34234

Gowda S, Weinstein DA, Blalock TD, Gandhi K, Mast BA, Chin G, Schultz GS (2015) Topical application of recombinant platelet-derived growth factor increases the rate of healing and the level of proteins that regulate this response. Int Wound J 5:564–571

Hattori H, Ishihara M (2017) Feasibility of improving platelet-rich plasma therapy by using chitosan with high platelet activation ability. Exp Ther Med 3:1176

Hu S, Bi S, Yan D, Zhou Z, Sun G, Cheng X, Chen X (2018) Preparation of composite hydroxybutyl chitosan sponge and its role in promoting wound healing. Carbohyd Polym 184:154–163

Jin J, Ji Z, Xu M, Liu C, Ye X, Zhang W, Li S, Wang D, Zhang W, Chen J (2018) Microspheres of carboxymethyl chitosan, sodium alginate, and collagen as a hemostatic agent in vivo. ACS Biomater Sci Eng 4(7):2541–2551

Jun EA, Lim KM, Kim K, Bae ON, Noh JY, Chung KH, Chung JH (2011) Silver nanoparticles enhance thrombus formation through increased platelet aggregation and procoagulant activity. Nanotoxicology 2:157–167

Kovach I, Rumschöttel J, Friberg SE, Koetz J (2016) Janus emulsion mediated porous scaffold bio-fabrication. Colloids Surf, B 145:347–352

Li JL, Zarbock A, Hidalgo A (2017a) Platelets as autonomous drones for hemostatic and immune surveillance. J Exp Med 214(8):2193–2204

Li Q, Niu Y, Diao H, Wang L, Chen X, Wang Y, Dong L, Wang C (2017b) In situ sequestration of endogenous PDGF-BB with an ECM-mimetic sponge for accelerated wound healing. Biomaterials 148:54–68

Li Z, Zhou F, Li Z, Lin S, Chen L, Liu L, Chen Y (2018) Hydrogel cross-linked with dynamic covalent bonding and micellization for promoting burn wound healing. ACS Appl Mater Interfaces 30:25194–25202

Liang D, Lu Z, Yang H, Gao J, Chen R (2016) A novel asymmetric wettable AgNPs/chitosan wound dressing: in vitro and in vivo evaluation. ACS Appl Mater Interfaces 6:3958

Long M, Zhang Y, Huang P, Chang S, Hu Y, Yang Q, Mao L, Yang H (2017) Emerging nanoclay composite for effective hemostasis. Adv Func Mater 10:1704452

Lu Z, Gao J, He Q, Wu J, Liang D, Yang H, Chen R (2017) Enhanced antibacterial and wound healing activities of microporous chitosan-Ag/ZnO composite dressing. Carbohyd Polym 156:460–469

Ma Y, Xin L, Tan H, Fan M, Li J, Jia Y, Ling Z, Chen Y, Hu X (2017) Chitosan membrane dressings toughened by glycerol to load antibacterial drugs for wound healing. Mater Sci Eng, C 81:522–531

Man WU (2018) Clinical efficacy of autologous platelet-rich gelatin in the treatment of patients with refractory diabetic skin ulcer and its effect on serum inflammatory factors. J Clin Med Pract 22:26–31

Mishra SK, Raveendran S, Ferreira JM, Kannan S (2016) In situ impregnation of silver nanoclusters in microporous chitosan-PEG membranes as an antibacterial and drug delivery percutaneous device. Langmuir ACS J Surf Colloids 40:10305

Mitra D, Li M, Wang R, Tang Z, Kang E-T, Neoh KG (2016) Scalable aqueous-based process for coating polymer and

metal substrates with stable quaternized chitosan antibacterial coatings. Ind Eng Chem Res 36:9603–9613

Nie W, Dai X, Li D, McCoul D, Gillispie GJ, Zhang Y, Yu B, He C (2018) One-pot synthesis of silver nanoparticle incorporated mesoporous silica granules for hemorrhage control and antibacterial treatment. ACS Biomater Sci Eng 10:3588–3599

Pourjavadi A, Soleyman R (2011) Silver nanoparticles with gelatin nanoshells: photochemical facile green synthesis and their antimicrobial activity. J Nanopart Res 10:4647–4658

Rodriguez-Menocal L, Shareef S, Salgado M, Shabbir A, Badiavas EV (2015) Role of whole bone marrow, whole bone marrow cultured cells, and mesenchymal stem cells in chronic wound healing. Stem Cell Res Ther 1:24

Sakoda M, Kaneko M, Ohta S, Qi P, Ichimura S, Yatomi Y, Ito T (2018) Injectable hemostat composed of a polyphosphate-conjugated hyaluronan hydrogel. Biomacromol 8:3280–3290

Sarhan WA, Azzazy HM, El-Sherbiny IM (2016) Honey/chitosan nanofiber wound dressing enriched with allium sativum and cleome droserifolia: enhanced antimicrobial and wound healing activity. ACS Appl Mater Interfaces 10:6379–6390

Seon GM, Hee LM, Kwon BJ, Sung KM, Koo MA, Kim D, Seomun Y, Kim JT, Park JC (2017) Functional improvement of hemostatic dressing by addition of recombinant batroxobin. Acta Biomater 48:175–185

Shi X, Fang Q, Ding M, Wu J, Ye F, Lv Z, Jin J (2016) Microspheres of carboxymethyl chitosan, sodium alginate and collagen for a novel hemostatic in vitro study. J Biomater Appl 7:1092–1102

Shi GN, Zhang CN, Xu R, Niu JF, Song HJ, Zhang XY, Wang WW, Wang YM, Li C, Wei XQ (2017) Enhanced antitumor immunity by targeting dendritic cells with tumor cell lysate-loaded chitosan nanoparticles vaccine. Biomaterials 113:191–202

Shimojo AAM, Perez AGM, Galdames SEM, Brissac ICS, Santana MHA (2016) Stabilization of porous chitosan improves the performance of its association with platelet-rich plasma as a composite scaffold. Mater Sci Eng, C 60:538–546

Smock KJ, Schmidt RL, Hadlock G, Stoddard G, Grainger DW, Munger MA (2014) Assessment of orally dosed commercial silver nanoparticles on human ex vivo platelet aggregation. Nanotoxicology 3:328–333

Sun X, Tang Z, Pan M, Wang Z, Yang H, Liu H (2017) Chitosan/kaolin composite porous microspheres with high hemostatic efficacy. Carbohydr Polym 177:135–143

Wang X, Yu T, Chen G, Zou J, Li J, Yan J (2017) Preparation and characterization of a chitosan/gelatin/extracellular matrix scaffold and its application in tissue engineering. Tissue Eng C Methods 3:169–179

Wang X, Guan J, Zhuang X, Li Z, Huang S, Yang J, Liu C, Li F, Tian F, Wu J, Shu Z (2018) Exploration of blood

coagulation of N-Alkyl chitosan nanofiber membrane in vitro. Biomacromol 3:731–739

Xia L, Xu M, Cheng G, Yang L, Guo Y, Li D, Fang D, Zhang Q, Liu H (2018) Facile construction of Ag nanoparticles encapsulated into carbon nanotubes with robust antibacterial activity. Carbon 130:775–781

Ye D, Zhong Z, Xu H, Chang C, Yang Z, Wang Y, Ye Q, Zhang L (2016) Construction of cellulose/nanosilver sponge materials and their antibacterial activities for infected wounds healing. Cellulose 1:1–15

Yoo J, Birke A, Kim J, Jang Y, Song SY, Ryu S, Kim BS, Kim BG, Barz M, Char K (2018) Cooperative catechol-functionalized polypept(o)ide brushes and Ag nanoparticles for combination of protein resistance and antimicrobial activity on metal oxide surfaces. Biomacromol 5:1602

Younes I, Sellimi S, Rinaudo M, Jellouli K, Nasri M (2014) Influence of acetylation degree and molecular weight of homogeneous chitosans on antibacterial and antifungal activities. Int J Food Microbiol 185:57–63

Zeng X, Mccarthy DT, Deletic A, Zhang X (2015) Silver/reduced graphene oxide hydrogel as novel bactericidal filter for point-of-use water disinfection. Adv Func Mater 27:4344–4351

Zhang L, Ma Y, Pan X, Chen S, Zhuang H, Wang S (2018) A composite hydrogel of chitosan/heparin/poly (γ-glutamic acid) loaded with superoxide dismutase for wound healing. Carbohydr Polym 180:168–174

Zhang K, Bai X, Yuan Z, Cao X, Jiao X, Li Y, Qin Y, Wen Y, Zhang X (2019) Layered nanofiber sponge with an improved capacity for promoting blood coagulation and wound healing. Biomaterials 204:70–79

Zhao X, Lang Q, Yildirimer L, Lin ZY, Cui W, Annabi N, Ng KW, Dokmeci MR, Ghaemmaghami AM, Khademhosseini A (2016) Photocrosslinkable gelatin hydrogel for epidermal tissue engineering. Adv Healthc Mater 1:108–118

Zhao X, Wu H, Guo B, Dong R, Qiu Y, Ma PX (2017) Antibacterial anti-oxidant electroactive injectable hydrogel as self-healing wound dressing with hemostasis and adhesiveness for cutaneous wound healing. Biomaterials 122:34–47

Zhao X, Guo B, Wu H, Liang Y, Ma PX (2018) Injectable antibacterial conductive nanocomposite cryogels with rapid shape recovery for noncompressible hemorrhage and wound healing. Nat Commun 9(1):2784

Zhu J, Li F, Wang X, Yu J, Wu D (2018) Hyaluronic acid and polyethylene glycol hybrid hydrogel encapsulating nanogel with hemostasis and sustainable antibacterial property for wound healing. ACS Appl Mater Interfaces 16:13304–13316